Structure dependent wear and shear mechanics of nanostructured MoS2 coatings

Peter Serles, Hao Sun, Guillaume Colas, Jason Tam, Eric Nicholson, Guorui Wang, Jane Howe, Aurélien Saulot, Chandra Veer Singh, Tobin Filleter

Structure Dependent Wear and Shear Mechanics of Nanostructured MoS_2 Coatings

Peter Serles, Hao Sun, Guillaume Colas, Jason Tam, Eric Nicholson, Guorui Wang, Jane Howe, Aurélien Saulot, Chandra Veer Singh, Tobin Filleter**

P. Serles, Dr. Guorui Wang, Prof. T. Filleter
Department of Mechanical & Industrial Engineering, The University of Toronto,
5 King's College Road, Toronto, ON, Canada, M5S 3G8
Email: filleter@mie.utoronto.ca

H. Sun, Dr. J. Tam, E. Nicholson, Prof. J Howe, Prof. C.V. Singh
Department of Materials Science and Engineering, The University of Toronto,
184 College St, Toronto, ON, Canada, M5S 3E4
Email: chandraveer.singh@utoronto.ca

Dr. G. Colas
Univ. Bourgogne Franche-Comté FEMTO-ST Institute CNRS/UFC/ENSMM/UTBM,
Department of Applied Mechanics, 24 rue de l'Epitaphe, F-25000 Besançon, France

Prof. A. Saulot
Université de Lyon, LaMCoS, INSA-Lyon, CNRS UMR 5259, France

Keywords: Nanocrystalline; Shear Failure; Molybdenum Disulfide; Friction Force Microscopy; Wear Rate

Abstract

Sputter deposited molybdenum disulfide coatings are one of the most common lubricants for extreme environments. However, their performance predictability remains limited by the complexity of van der Waals wear and shear mechanics in bulk materials resulting in unexpected premature failure. In the present study, two nanostructured MoS_2 coatings of similar macroscopic properties are shown to exhibit entirely different wear and shear mechanics due to their nanostructure. Friction force microscopy with steel-beaded cantilevers is used to measure the per-cycle evolution of friction, wear, and topography *in* situ over the lubricant lifetime under an inert nitrogen environment. Molecular dynamics simulations confirm the subsurface structural failure mechanisms of the coatings under shear stress and AFM phase imaging and Raman spectroscopy are used to identify tribofilm formation mechanics. The nanocrystal-amorphous composite structure shows improved wear resistance but at the cost of limited stress relaxation which creates high-stress failure and fracture-dominated wear. The purely nanocrystalline coating exhibits lower shear resistance but consistent stress relaxation by van der Waals cleavage and triple junction fracture which results in higher wear rates with predictable abrasion-dominated failure. The contrast in nanoscale performance of the coatings allows for the lubricant nanostructure to be tuned for ideal applications for extreme environments.

1. Introduction

Molybdenum disulfide has been used as one of the most common lubricants in extreme environments such as the space industry and self-lubricating cutting tools for more than 50 years.[1,2] Despite this history, the performance of this lubricant under different loading and environmental conditions continues to remain unpredictable. The complexity of the system including structural deformation, tribo-chemical reactivity, fracture and wear mechanics, and a constantly evolving contact have led to ongoing difficulty in understanding the performance of these micron-thick lubricant coatings under shear stresses.[3,4] In the space industry, this has resulted in premature and unexpected failure of satellites, rockets, and telescopes costing billions of dollars over the past several decades.[5–7] Predictable performance of these bulk van der Waals solid lubricant materials depends on the fundamental understanding into their lubricating mechanics over the wide variety of environments that they will face. Certain mechanical and material characteristics are beginning to be better established including coating structures,[4,8,9] tribochemical interactions,[10] tribofilm rheology,[11,12] and fracture mechanics,[13] however, the basic evolution and failure modes of the contact including wear, shear deformation, and breakdown mechanics still remain poorly understood. The primary reason for this poor understanding is a lack of *in situ* detection techniques; the most common method to evaluate wear and failure behaviour is simply to compare the *post mortem* wear surface to the virgin condition of the lubricant.[14–16] Certain *in situ* techniques such as transparent contacts allow for monitoring of the evolution[11,17] but use transparent materials therefore changing the contact conditions and limiting relevance to the application. *In situ* Raman[18] and mass spectrometry[3,19] detect tribochemical changes but provide little understanding of the mechanical performance. However, atomic force microscope (AFM) based friction force microscopy (FFM) was recently used to identify the growth rate of a ZDDP film *in situ* while undergoing friction stimulation.[20] This topographic measurement concurrent

with friction is therefore extended in the present study to measure the change in topography when FFM is employed in the wear regime, providing an *in situ* wear rate measurement.

A major contribution to the lack of predictability in MoS_2 coatings is the variability of different nanostructures between different coatings. Historically, MoS_2 lubricant coatings have shown preference for crystalline over amorphous structures since the long-range order of van der Waals bonded lamellae in the (002) direction allows for easy "deck of cards" internal shear between sheets creating ultra-low friction lubricants.[3,21] However, the weak bonding of van der Waals layers also makes MoS_2 highly susceptible to wear. To improve the wear life of these coatings, MoS_2 was co-sputter deposited with harder metal and non-metal additives[22] and the crystal size was reduced to the nanoscale to improve yield strength following the Hall-Petch relation.[23] A few co-deposited additives have shown improved lubricating properties under certain environments,[24] but the lack of predictability into failure mechanisms of pure MoS_2 coatings has continued to hamper their performance. Nanocrystalline MoS_2 coatings have also shown promise. But, while analogous wear-resistant metal coatings have shown unique nanostructure-dependent properties,[25,26] the unique structural characteristics of MoS_2 and other van der Waals materials requires specific study. Investigations into the in-plane strength of nanocrystalline monolayer MoS_2 found a clear dependence of nanocrystal size on the strength,[27] but the influence of multi-layer nanocrystalline structure in van der Waals materials remains unknown. In order to understand and predict the operation and failure mechanics of MoS_2 and other van der Waals structured coatings, the evolution and failure mechanics must be understood in the context of the coating nanostructure. In the present study, two MoS_2 coatings of unique nanostructures are subjected to friction force microscopy in the wear regime to detect the per-cycle wear rates *in situ* as well as molecular dynamic simulations to identify the structural lubricating and breakdown mechanics under shear stress. Despite similar

macroscopic properties, the unique nanostructures of the two coatings are found to largely influence the coating shear characteristics leading to entirely different lubricating mechanics.

2. Results & Discussion

2.1. Nanostructural Characterization

Two sputter-deposited 1µm thick MoS_2 lubricant coatings exhibiting distinct nanostructures are evaluated; the first coating is purely nanocrystalline in nature, and the second consisting of nanocrystals embedded in an amorphous matrix. **Figure 1** shows the material characteristics including cross-sectional high-resolution transmission electron microscopy (HRTEM) images, X-ray diffraction (XRD) spectra, selected area electron diffraction (SAED) patterns, and molecular dynamics (MD) models representing these two coatings. The first coating is composed of a completely nanocrystalline structure (MoS_2-nc, Figure 1 a) with crystal sizes of M=5.6±1.8 nm in the major axis (a=b=3.15 Å, (100) or (010) directions, covalently bonded in-plane) and m=6.6±2.2 nm in the minor axis (c=6.15 Å, (001) direction, van der Waals bonded out-of-plane). XRD and SAED of MoS_2-nc (Figure 1 c, e) confirm the entirely crystalline structure with a slight texture. Based on this grain size, MoS_2-nc has an intergranular volume of 42% (*cf.* SI1). The second coating shows a structure of nanocrystals embedded in an amorphous matrix (MoS_2-am, Figure 1 b) with more elongated crystal dimensions of M=11.8±2.3 nm and m=3.3±0.8 nm. Areal analysis of HRTEM micrographs suggests 30-40% nanocrystalline phase within 60-70% amorphous matrix which agrees with XRD and SAED patterns (Figure 1 d, f). 2 nm cross-sectional slices of the MD unit cells for the two coatings are presented in Figure 1 g, h. The MoS_2-nc unit cell (Figure 1 g) consists of a randomly oriented polycrystalline cell with mean crystal size of 6 nm and the MoS_2-am (Figure 1 h) cell contains of an embedded crystal of 12 nm by 3 nm in an amorphous matrix representing 35% and 65% of the unit cell volume respectively. Additionally, Young's modulus and hardness of the

coatings were measured by nanoindentation and surface roughness was measured using atomic force microscopy (AFM) topographic imaging (Table SI1). While surface roughness,[28,29] hardness,[30] and Young's modulus[31] are known to affect friction and wear performance, the mechanical properties of the two coatings were found to be similar therefore suggesting limited effect of these parameters.

2.2 Friction and Shear Mechanics

The two coatings were subjected to repeated friction force microscopy (FFM) tests under inert dry nitrogen using custom AFM cantilevers with AISI 440C steel bead contacts as shown in **Figure 2** a. The tests of 1024 linear reciprocating cycles were performed under high normal loads of 30-35 μN corresponding to 1 GPa contact pressure (*cf.* SI2) leading to wear profiles as depicted in the AFM projection and schematic of Figure 2 b and 2 c respectively. Repeated tribological tests were performed on each sample (*cf.* SI3) and the median coefficient of friction for each coating with the respective tribological characteristics as a function of cycle number are presented in Figure 2 d-k. The per-cycle coefficient of friction (CoF) for MoS_2-nc and MoS_2-am is shown in Figure 2 d, e respectively. The topographic signal which is generated during FFM is filtered into 2D line topography and average depth signals (*cf.* SI4) shown as wear track roughness (Rms) in Figure 2 f, g and cross-sectional wear volume per μm travelled (ΔVol/μm) in Figure 2 h, i respectively. The derivative of the wear rate, the wear/cycle, is shown in Figure 2 j, k along with the 10-cycle moving average in red.

Both coatings are very strong lubricants with CoF below 0.1 on average but it is immediately apparent that the per-cycle behaviour is drastically different. MoS_2-nc exhibits a relatively steady friction behaviour throughout all 1024 cycles but MoS_2-am displays an erratic behaviour with many deviations from the mean. As the macroscopic mechanical properties of the two coatings were found to be similar, the difference in friction behaviour is therefore suggestive

of differences in the coating structure and their ability to handle shear deformation. Considering the friction, roughness, and wear evolution of the two coatings, a few distinct relationships can be noted. The initial FFM cycles for both materials show a decrease in roughness correlating closely with a decrease in CoF which is consistent with conventional run-in theories.[29,32] It is also proposed that the changes in roughness throughout the evolution are influenced by the wear characteristics as two mechanisms can be considered: gradual wear can decrease roughness by locally leveling peaks and filling valleys, but aggressive wear can yield an opposite effect by fracturing the smooth surface or protective tribofilm to expose a rougher underlying topography. The first mechanism is indicated by the run-in wear rate which is an order of magnitude greater for both coatings during the first 50 cycles compared to the remaining 974 cycles (*cf.* Figure 2 h-k). For MoS_2-nc, this corresponds to a 49% decrease in the Rms over the first 50 cycle run-in period compared to only a 12% decrease in Rms during the remaining steady state period (*cf.* Figure 2 f, g). The second wear mechanism can be seen throughout the steady state behaviour of MoS_2-am which, at cycles 414, 454, 732, 803 and 876, presents statistically outlying per-cycle wear rates (Figure 2 k noted with red arrows) compared to the average cycles (*cf.* SI5). This is evidence of major wear events happening in the coating. Interestingly, for all but one of these five spikes in per-cycle wear rate, a corresponding spike in both the Rms and CoF on the subsequent cycle occurs (i.e. ΔVol/cycle spikes on cycle 732 then Rms and CoF spike on cycle 733, *cf.* SI5). This confirms the direct causal relationship where the wear fracture events create a rougher surface which therefore increases friction.

While CoF, roughness, and wear have clear ties throughout the tribological evolution, a few relationships remain unexplained. Higher average surface roughness is typically associated with higher CoF,[28,29] yet, despite the steady state roughness of MoS_2-nc being 14% lower than MoS_2-am, the steady state friction is 45% greater ($Rms_{MoS_2\text{-}nc}$=3.50±0.1 nm vs. $Rms_{MoS_2\text{-}am}$=4.04±0.06 nm; $\mu_{MoS_2\text{-}nc}$= 0.061±0.006 *vs*. $\mu_{MoS_2\text{-}am}$= 0.034±0.006). Furthermore, it is well

known that interlayer shear of van der Waals layers is responsible for the superlubricious behaviour of MoS_2,[10,33,34] so conventional wisdom suggests that the dominantly-crystalline MoS_2-nc would boast a lower CoF. However, it is also well known that the interlayer sliding occurs predominantly in basal oriented planes which are parallel to the direction of sliding[8,9,35,36] while the MoS_2-nc sample features a range of crystal orientations. Furthermore, crystals which are not basally oriented may in fact impede the movement of the crystals which are oriented favourably to sliding as their strong covalent in-plane bonding would act as a barrier. Conversely, the disordered bonding and abundance of voids both within and at the interface of the amorphous matrix can create a more compliant structure which would reduce resistance to shear deformation in the MoS_2-am structure.

In order to identify the effect of intrinsic coating structure on compliance under shear, 3D molecular dynamics (MD) simulations under shear loading with periodic boundary conditions have been developed. **Figure 3** shows 2 nm thick slices of the four different configurations: single-crystal MoS_2 (Figure 3 a), two MoS_2 crystals oriented 90º to each other (Figure 3 b), a nanocrystal embedded in an amorphous matrix as per MoS_2-am (Figure 3 c), and randomly-oriented polycrystalline with 6 nm average grain size as per MoS_2-nc (Figure 3 d). The single-crystal, bi-crystal, and amorphous matrix unit cells are 11x25x10 nm in x,y,z with the (100) plane oriented to the direction of shear (except for the right half of the bi-crystal which is 90º). The nanocrystalline unit cell is 24x24x24 nm in x,y,z in order to achieve true random directionality of the nanocrystals. Figure 3 e shows the shear stress vs. shear strain curves of the four configurations. Ultimate shear stress (USS) is noted with stars on the curves and is defined as the maximum stress before softening. The inset of Figure 3 e inset shows the linear-elastic regime from which the shear modulus, G, is measured to 2% elastic shear strain. It should be noted that the present MD configuration faces inherent limitations as it does not represent the entire tribological contact of steel sliding on MoS_2 with tribofilm formation, wear ejection,

tribochemical effects, and other dynamic tribological factors. Additionally, the strain rate is several orders of magnitude greater than experimental values. However, by subjecting the two coatings to identical strain conditions and isolating the intrinsic coating response under shear stresses, the otherwise undetectable subsurface response of the differently structured MoS_2 coatings can be identified. Full videos showing the MD shear deformation of the four unit cells to failure is available in the Supporting Information video file.

The shear deformation behaviour of the single and bi-crystals demonstrate that the addition of a 90º misorientation between planes drastically increases the resistance to shear as the shear modulus is estimated to be two orders of magnitude greater for the bi-crystal as opposed to the single crystal. Furthermore, the end condition for the single crystal cell in Figure 3 a shows a smooth gradient of shear deformation while the end condition of the bi-crystal in Figure 3 b exhibits discontinuous sliding. This discontinuous sliding behaviour correlates with the serrated flow of the bi-crystal stress-strain curve which shows stress jumps corresponding with the breaking of covalent bonds at the interface between crystals. In the bi-crystal, the shearing of horizontally oriented layers only occurs after the breaking of these interfacial bonds while the vertically oriented planes are not found to exhibit any sliding. Instead, the sliding of horizontal layers compresses the vertically oriented planes resulting in the vertical planes buckling out of plane. This confirms that the shearing of van der Waals layers in single crystal MoS_2 requires both the parallel orientation of the planes as well as an unconstrained geometry by surrounding structures.

The deformational behaviour of MoS_2-am and MoS_2-nc simulated cells shown in Figure 3 c and d respectively depict very different shear mechanisms. The shear modulus of the MoS_2-am cell is found to be 21% lower than the MoS_2-nc cell which represents a lower shear stress for the same elastics strain and therefore a lower structural resistance to shear deformation. This is

in agreement with the lower average coefficient of friction for MoS_2-am as per Figure 2 a, b. Meanwhile, the USS of MoS_2-nc is found to be 15% lower than MoS_2-am and occurs at 20% lower shear strain comparatively. The wear volume of a material is considered to be inversely proportional to USS as per Equation (1):[37,38]

$$V = K \frac{F}{USS} L \quad (1)$$

Where V is the wear volume, F is the friction force, L is the contact length, and K is a dimensionless proportionality constant which is the probability of removing a wear particle. The lower USS of MoS_2-nc is therefore in agreement with the increased wear rate in the FFM measurements as per Figure 2 h-k.

The lower shear modulus of MoS_2-am can be attributed to the symbiotic relationship between the two phases as seen in Figure 3 c. The disordered nature of the amorphous matrix allows for greater compliance and therefore both van der Waals shear of the crystal and grain rotation within the matrix are observed. Conversely, the MoS_2-nc cell is much more rigid under deformation which leads to cracks opening at the grain triple junctions (circled in the enlarged sections of Figure 3 d). Similar to the bi-crystal behaviour, van der Waals sliding is only seen once a void is created next to horizontally oriented sheets; the triple junction which fails in the second frame of Figure 3 d (circled in yellow) allows for the adjacent planes to slide as noted in the third frame. It can also be seen in the second frame that following the triple junction failure, crack propagation proceeds along both the grain boundary to the left and by cleaving the MoS_2 planes below. Finally, plane buckling is noted (black circle in the third frame) similarly to the bi-crystal mechanism of out-of-plane buckling when confined by other grains. The rigidity of the nanocrystalline structure and limited van der Waals sliding therefore likely leads to the greater shear modulus and thus CoF. While crystalline MoS_2 structures have been conventionally considered the lower friction coating to amorphous coatings,[3,4,21] it is seen that

only well-oriented and unrestricted van der Waals planes are able to capitalize on the easy shearing characteristic. The densely bound grain structure of nanocrystalline MoS_2-nc is actually found to reduce shear compliance when compared with MoS_2-am thus increasing the shear modulus and friction coefficient and reducing the USS and wear resistance.

Considering the elasticity relation for bulk isotropic materials,[39] and the Poisson's ratio of MoS_2 as ν=0.27,[13,40] the shear modulus determined by MD simulation for MoS_2-nc, $G_{MoS2\text{-}nc}$=21.1 GPa, is in agreement with the Young's modulus measured by nanoindentation, $E_{MoS2\text{-}nc}$=54.4 ± 2 GPa (*cf.* SI1). However, the MoS_2-am coating is anisotropic with the embedded crystal aligned with the shear loading which results in a discrepancy between the estimated shear modulus and the measured Young's modulus. The validated shear modulus for MoS_2-nc, as well as the corresponding trends of G with μ and USS with V, help to ensure confidence in the MD simulations to identify the subsurface shear mechanics of these coatings."

2.3 *In Situ* Wear Behaviour

The failure mechanics and wear behaviour of the lubricants are similarly found to depend on the structure of the coating. The steady state friction, and therefore interfacial shear, of MoS_2-nc is ~80% greater than MoS_2-am but the total wear volume is more than 170% greater. Additionally, the mechanisms behind the coating wear are entirely different. MoS_2-nc demonstrates "abrasion-dominated" wear with stable wear rates and minimal deviation from the mean while MoS_2-am presents "fracture-dominated" wear with low wear rates on average cycles but random cycles showing statistically outlying extreme wear. As the FFM contact parameters and environmental conditions are the same and mechanical properties of the two coatings are similar, it is considered that the wear mechanics of MoS_2 coatings also depend on their structure.

The wear mechanics of the MoS_2-am coating is found to be analogous to that seen in nanocrystal-amorphous metals which have been shown to present greater wear resistance than either purely nanocrystalline or amorphous metals[41,42] due to the symbiotic relationship between the phases. In metals, cracks and shear bands that propagate through the amorphous regions have been shown to halt and delocalize upon reaching nanocrystals,[43–45] while the inherently flawed and ductile amorphous matrix provides a tolerance for incoherency strain from nanocrystal growth[46] and shear-induced nanocracks.[44] Previous work examining the fracture propagation of the MoS_2-am coating agrees with this failure mode as the fracture surface showed a multifaceted nano-topography suggesting random redirection of cracks by nanocrystals.[13] While this symbiotic relationship provides greater wear resistance, when the USS is reached, this corresponds with high internal stress and significant fracture-dominated wear occurs. The estimate by MD simulations is in agreement as the USS of MoS_2-am is 21% higher than MoS_2-nc as well as occurring at 20% greater strain (Figure 3 e). This fracture-wear event then exposes the rougher underlying surface leading to the aforementioned spikes in roughness and CoF on the following cycle (Figure 2 e, g). Popov *et al.*[47] noted similar trends in a coating of nanocrystal diamond suspended in amorphous carbon where the average CoF was μ_{avg}=0.1 with spikes as high as μ=0.6. Conversely, for MoS_2-nc, the weak bonding between van der Waals layers as well as the abundance of grain boundaries containing voids and defects produces points of failure through cleavage of lamellae and grain boundary fracture resulting in lower wear resistance during shear. This is in accord with MD simulations which present coating failure in the 6 nm polycrystalline cell beginning at triple junctions and propagating between layers and along grain boundaries. The USS of MoS_2-nc is estimated to be lower and occurs at a lower strain compared to the MoS_2-am cell which agrees with the significantly greater wear volume. However, this also allows for greater stress relaxation of MoS_2-nc and thus steadier and more predictable abrasion-dominated wear and friction behaviour.

As the two coatings present two very different wear regimes, it is expected that the wear debris would be very different; abrasion-dominated wear particles from MoS_2-nc should be small and plentiful while fracture-dominated wear particles from MoS_2-am should be large and fewer.

Figure 4 a, b shows high-resolution scanning electron microscopy (HRSEM) images of the ejected wear particles for a square friction test after 150 cycles (additional micrographs in SI6). The debris in Figure **4** a from MoS_2-nc are compacted sheets which appear to consist of many smaller particles while the wear debris in Figure **4** b from MoS_2-am are large and randomly shaped. This follows the third-body theory which states that **"**big and/or brittle particles are ejected while small particles are agglomerated inside the contact".[11,48–50] The abrasion-dominated wear of MoS_2-nc thus produces smaller particles that are trapped inside the contact and compacted into sheets while the fracture-dominated wear of MoS_2-am produces wear particles which are too large to be trapped in the contact and are ejected. These wear regimes would either feed or starve the tribofilm of small particles to agglomerate so we would additionally expect to see entirely different run-in and tribofilm mechanics between the two coatings.

2.4 Run-In and Tribofilm Mechanics

The characteristics of the run-in phase as well as the steady state formation of a protective tribofilm can be similarly traced to the coating structure. Figure **4** c-f shows 3D plots of the friction and wear track topography for first 200 cycles of the same tribological tests as Figure 2. The *x* axis shows the 60 µm reciprocating horizontal sliding distance for each cycle with the cycle number on the *y* axis. The *x* axis contains 1024 pixels or one data point every 58 nm of sliding. For MoS_2-nc, the topography and friction in Figure **4** c, e respectively show very similar behaviour including higher topographic and friction

peaks at the same horizontal sliding coordinate. As previously discussed, higher roughness correlates with higher friction, but we further note that during the first 50 cycles both signals decrease similarly at respective horizontal sliding coordinates. This confirms that the reduction of friction during run-in is directly correlated with the localized leveling of peaks and filling of valleys as is discussed. Conversely, MoS_2-am shows a much shorter run-in period of 22 cycles but quickly experiences spikes in local topography and friction as seen in Figure **4** d, f. At cycle 86, a small fracture event occurs which corresponds to a decrease in localized topography during cycles 86-120 as well as a sudden increase in localized friction beginning on cycle 87 at the same horizontal coordinates. This shows that the fracture wear is a surface level effect which only affects a localized 35 µm of the 60 µm track and removes approximately 5 nm of material depth which corresponds closely to the nanocrystal size.

While the evolution during early run-in cycles is dominated by roughness changes, steady state operation is governed by other mechanisms. As noted, for MoS_2-nc the roughness decreases by 49% during the first 50 cycles and friction decreases by 27% accordingly. However, during the following 974 cycles the roughness only decreases by 12% and yet the friction decreases by another 26%. Conversely, for MoS_2-am, the mean value for friction and roughness in the 50 cycles following run-in and the final 50 cycles are statistically similar suggesting little evolution throughout. Therefore, following run-in, the tribological mechanisms begin to be influenced by additional factors that are unique to the individual coating. To identify changes in the wear track including the commonly identified protective tribofilm,[10,19] AFM tapping mode imaging can be used to generate spatial phase images. Phase imaging depends on the cantilever-sample damping and can detect changes in the contact adhesion and stiffness across spatial regions so is often employed to detect tribofilm formation.[51,52] **Figure 5** a-f shows phase images of the wear tracks following 128, 256, and 1024 cycles for the two coatings. By cycle 128, both coatings show only minimal phase contrast and therefore little tribofilm

development. However, MoS_2-nc begins to show more significant phase contrast at cycle 256 and shows complete phase coverage by cycle 1024 as per Figure 5 a-c. MoS_2-am, however, fails to develop a tribofilm throughout the entire 1024 cycles. Additionally, the transfer film onto the AISI 440c steel bead countersurface is found to be more coherent with a larger volume on the bead used for MoS_2-nc as compared to MoS_2-am at the end of 1024 cycles (*cf.* SI7).

Raman spectroscopy was additionally used to identify the difference in vibrational modes inside and outside of the wear track for the two coatings and can be seen in Figure 5 g, h. The two predominant peaks for 2H MoS_2 are present at ~372 cm^{-1} and ~404 cm^{-1} representing E^1_{2g} and A_{1g} first order Raman vibrational modes respectively. E^1_{2g} mode corresponds with the in-plane vibration of MoS_2 in the (100) plane while A_{1g} mode corresponds to out-of-plane vibration in the (002) direction.[53] Additionally, the LA(M) peaks can be seen from 190-230 cm^{-1} which correspond to the disorder and defects present in MoS_2.[53] It should be noted that amorphous MoS_2 is not Raman active and provides a very weak spectrum that cannot be distinguished in MoS_2-am so the resulting spectrum of MoS_2-am is characteristic only of the 30-40% nanocrystalline volume.[54] **Table 1** shows the full width at half-maximum (FWHM) as well as the peak location for both E^1_{2g} and A_{1g} as well as the normalized integral peak intensity for LA(M) for all four samples.

The FWHM of both peaks for MoS_2-am increase inside the wear track compared to the pristine coating while the FWHM decreases for both peaks in the MoS_2-nc wear track. Considering the phonon confinement effect, FWHM is found to be inversely proportional to the grain size for MoS_2.[55] This suggests that FFM has induced structural changes in the coating or tribofilm. For MoS_2-am, the notable increase in FWHM of E^1_{2g} peak suggests smaller grains in the (100) direction which could be due to fracture or stress-induced crystallization of smaller

grains. In MoS_2-nc, the tribofilm shows a slight decrease in FWHM which may be due to crystallization or stress-induced reorientation of the tribofilm towards a tribologically favourable basal configuration. Additionally, the intensity of the LA(M) disorder peak in the wear track increases more significantly for MoS_2-am than MoS_2-nc suggesting a higher degree of stress induced disorder in the coating.

The E^1_{2g} peak is also found to split for both coatings which can be attributed to the internal strain of the surface. The MoS_2-am E^1_{2g} peak in the wear track is found to twin as per Figure 5h with the secondary peak occurring at 350 cm^{-1}. Peak splitting is typical of uniaxial strain with the two peaks polarized parallel and perpendicular to the direction of strain.[56,57] In particular, the secondary peak occurring at around 350 cm^{-1} accounts for the vibration along the direction of the tensile strain.[57] This strain-driven peak splitting of MoS_2-am is in agreement with the fracture-dominated wear regime noted for the coating due to higher internal strain upon failure as per the wear behaviour and MD simulations. Comparatively, a distinct secondary peak can be noted for MoS_2-nc at 346 cm^{-1} which is also likely due to uniaxial strain, however, the peak is much less significant confirming lower internal strain in agreement with the wear mechanisms and MD simulations. A final consideration is the formation of of MoO_3, the dominant oxide of MoS_2 which impedes lubrication, can be identified by Raman peaks occurring at ~820 cm^{-1} and ~980 cm^{-1}.[58] However, these peaks are not present beyond the background signal collected in the spectrum suggesting no tribologically driven oxide formation in the present nitrogen environment.

The distinct tribofilm and crystallization of the MoS_2-nc wear track compared to the lack of tribofilm and internal strain of MoS_2-am are suggestive of two entirely different surface states at the end of the 1024 FFM cycles. The wear particles noted in Figure **4** and the internal strain state of Figure 5 explains the tribofilm discrepancy as the

fracture-dominant wear particles of MoS_2-am are too large to remain in a contact of this scale which starves the tribofilm development.[11,18] Additionally, any tribofilm that may begin to grow on MoS_2-am from the amorphous content would likely be removed along with the subsurface material during major fracture events due to the internal strain. Conversely, the particles created by MoS_2-nc are much smaller due to the lower USS and are agglomerated in the contact forming a cohesive tribofilm with increased crystallographic order. This progressive surface evolution throughout the 1024 cycles therefore impacts the behaviour for both coatings: progressive tribofilm development leads to a steadily decreasing CoF for MoS_2-nc while the CoF remains constant for MoS_2-am as no tribofilm is formed. Friction contacts are indeed very convoluted systems with differing mechanisms between run-in and steady state operation as well as widely different mechanisms between coating nanostructures despite similar macroscopic properties.

3. Conclusions

Two nanostructured molybdenum disulfide solid lubricant coatings have been investigated which exhibit extremely attractive tribological properties for lubricating steel contacts including a CoF below 0.1 and extensive wear lives. The coatings, however, achieve these strong lubricating properties through entirely different shear and wear mechanics. The MoS_2-am nanocrystalline-amorphous matrix coating has a lower average friction coefficient by 55% and offers intrinsic coating-driven lubrication. As revealed by MD simulations, the structure's favourable shear modulus depends on both van der Waals sliding as well as a synergistic relationship between crystalline and amorphous phases. The coating performance has little dependence on tribofilm formation and so achieves steady state behaviour in as few as 22 cycles during FFM. However, while MoS_2-am demonstrates lower average friction and wear behaviour, when the coating fractures it does so in a catastrophic manner due to high

internal stresses. This strips the friction track of any tribofilm formation and disrupts the friction and topographic characteristics at the FFM scale. The resulting lack of tribofilm and internal stresses are collectively detected by surface measures of AFM phase imaging and Raman spectroscopy. Contrarily, the purely nanocrystalline MoS_2-nc has a 21% lower shear strength and therefore limited wear resistance due to the high proportion of triple junctions and van der Waals planes which easily fracture and cleave respectively. This lower ultimate shear strength occurs at 20% lower internal strain as observed in MD simulations and is in accord with the 170% greater amount of wear generated during FFM. This poorer wear resistance, however, leads to wear behaviour that is abrasive due to easy crack propagation and is therefore predictable and less destructive on average cycles. Additionally, these wear particles for MoS_2-nc are smaller and can be trapped inside the contact leading to the formation of a significant tribofilm. This tribofilm is found to consist of an improved crystallographic order compared to the pristine coating and is coherent by the end of 1024 cycles. This means that MoS_2-nc takes much longer to reach its steady-state behaviour but presents friction and wear behaviour that remains consistent and predictable throughout its lifetime.

This further understanding of the lubricating behaviour allows better prediction and design of lubricants for specific application including self-lubricating tools and space mechanisms. The testing conditions were selected to be comparable with mechanism-scale applications (contact pressure, space-grade steel, N_2 environment, *etc.*) which allows the validation of FFM with application-specific performance. This resulted in statistically similar average friction coefficients and similar topography of wear debris (*cf.* SI8). It should be noted however that while the magnitude of friction is in agreement between the scales, the macro-tribological testing shows much smoother curves as the contact is averaged across large volumes. This presents the benefit as well as limitations of FFM: nanoscale detection is able to determine the discrete mechanisms which contribute to the overall wear and failure behaviour, but the

magnitude of disturbances which are created in the system are over-exaggerated compared to the real application. Further discussion of cross-scale comparison can be found in SI8. Using the present understanding of the lubricant performance and breakdown mechanics, we are able to better establish the reason for discrepancies and uncertainties in macroscale performance of these coatings and the lubricant structure can be tailored to the specific mechanism for extreme applications.

4. Experimental Methods

4.1 Material Synthesis

Both coatings were deposited by direct-current magnetron sputtering on (100) N-doped silicon wafers with a 285 nm SiO_2 top layer. Both coatings were deposited to thicknesses of 1.1 μm using space-qualified deposition systems that were free of contaminants. The MoS_2-am coating was deposited by Blösch AG. Grenchen, Switzerland and the MoS_2-nc coating was deposited by Teer Coatings Ltd., Droitwich, UK.

4.2 Friction Force Microscopy

Friction force microscopy tests were carried out using an Asylum MFP-3D Classic AFM in contact mode using custom cantilevers. The cantilevers were prepared by attaching ~10 μm diameter AISI 440c stainless steel beads (Sandvik Osprey Ltd.) to NANOSENSORS Tipless Silicon cantilevers of 60 ± 8 N/m stiffness. The FFM tests were performed under pure flowing nitrogen environments (<2% RH, 99.9% purity N_2, Linde plc.) using a custom environmental control box within the AFM enclosure. The normal force was determined to correspond to 1 GPa contact pressure (*cf.* SI2), while contact velocity was set to 0.25 Hz or 15 μm/s. The cantilever normal[59] and lateral[60] stiffness calibration was performed as per the respective Sader methods with a factor of 2 for trapezoidal cantilevers and lateral sensitivity as per the test

probe method.[61] The coating surface was first imaged in tapping mode to find an area free of debris and damage, after which the cantilever was positioned for a 60 μm long, single-wide wear track in reciprocating linear contact. The normal force was held constant and the Asylum software recorded normal, and bi-directional lateral signals. The cantilevers were cleaned between each test to remove wear debris particulate by AFM-driven vibration at 1 MHz in acetone and ethanol for 10 minutes. This cleaning procedure was found to remove all wear debris and produce statistically similar friction curves following cleaning as pristine unused cantilevers.

4.3 Microscopy & Diffraction

High-resolution transmission electron microscopy images and selected area electron diffraction patterns were captured using a Hitachi HF3300 (Figure 1). Two samples of each coating were evaluated with thicknesses ranging from 65-82 nm using accelerating voltage and emission currents of 300 kV and 5 μA respectively. The accelerating voltage and current were selected based on comparable literature[62,63] and appropriate precautions were taken to minimize electron-induced artifacts. The HRTEM samples were prepared using a Hitachi NB5000 high precision dual-beam FIB and SEM as per standard lift-out procedure.[13,64] X-ray diffraction (Figure 1) was performed using a Rigaku MiniFlex 600 X-ray diffractometer equipped with a 2.0 kW Cu X-ray tube with corresponding wavelength λ=1.5406 Å. The scanning range was 10-80º and the tests were performed at 1º/min (2θ). Topographic and phase (Figure 5) AFM imaging was performed using an Asylum MFP-3D Classic AFM in tapping mode using NANOSENSORS POINTPROBE-PLUS® Silicon-SPM-Sensor sharp-tip cantilevers of 64±4 N/m stiffness. High-resolution scanning electron microscopy images (Figure **4**) were generated using a Hitachi SU5000 with secondary electron imaging operating at 5 kV. High-frequency Raman measurements were performed using a Renishaw InVia Raman microscope with an incident wavelength of 532 nm from a diode-pumped solid-state laser. The

spectral resolution was ~1.9 cm^{-1} and the spatial resolution was ~1 μm. The laser intensity was maintained at 5% or 2 mW to avoid local heating induced by the laser. The penetration depth of the Raman laser in MoS_2 is wavelength-dependent and estimated to be around 38 nm in case of the 532 nm laser.

4.4 Molecular Dynamics Simulations

All simulations were performed using LAMMPS[65] and a 1-fs timestep. A reactive-empirical-bond-order (REBO) potential was used to describe the interatomic interactions of MoS_2.[66] This potential has been used before to study the mechanical properties of MoS_2.[67,68] The single-crystal, bi-crystal, and amorphous matrix unit cells were 11x25x10 nm in x,y,z with the (001) plane oriented to the direction of shear (except for the right half of the bi-crystal which is 90º). The nanocrystalline unit cell is 24x24x24 nm in x,y,z which was increased periodically until true random directionality of the nanocrystals was achieved. Voronoi tessellation[69] was used to create the nanocrystalline structure of MoS_2 in which each grain has a randomly-chosen orientation. All models were initially relaxed at zero pressure, zero temperature by the conjugate gradient algorithm[70] and then gradually increased to 300 K based on the Nose-Hoover, isothermal-isobaric ensembles in 100 ps. The amorphous structure was created by heating the MoS_2 until melting, then quickly cooling it down to 300 K in 100 ps. Strain-controlled shear deformation was emulated at a shear rate of 10^9/s at 300 K. Strains were applied by i) changing the angle between the *z* and *y* axes of the simulation cell so the shape of the simulation cell is varied, ii) an equal affine transformation was applied to all atomic positions, iii) the deformed models were subjected to isothermal-isobaric (NPT) relaxation in the *x* axis perpendicular to the sheared *yz* plane. The cell dimensions in the *z* and *y* axis were held constant during the relaxation to preserve the overall shear strain. The relaxation time thus determines the strain rate.

Supporting Information

1. Supplementary Information as referenced, PDF file.

   SI1 – Coating Characterization

   SI2 – Spherical Probe Contact Mechanics

   SI3 – Statistical Dataset of Tribological Results

   SI4 – Roughness and Depth Filtering

   SI5 – Statistical Significance of MoS_2-am Fracture-Wear Events

   SI6 – Additional Micrographs of Wear Debris Following 150 Cycles

   SI7 – Transfer Film on AISI440c Steel Bead

   SI8 – Space Mechanism Similarity

2. Video of molecular dynamics shear deformation of the four unit cells, .mp4 file.

Acknowledgements

Funding for this work was provided by the Erwin Edward Hart Professorship at the University of Toronto, MITACS Canada, The Natural Sciences and Engineering Research Council of Canada, and the Canadian Foundation for Innovation.

S. Boccia of the Ontario Centre for the Characterization of Advanced Materials (OCCAM) and R. Acosta of the Walter Curlook Materials Characterization & Processing Laboratory provided excellent guidance and technical support during the material characterization in this work.

Received: ((will be filled in by the editorial staff))
Revised: ((will be filled in by the editorial staff))
Published online: ((will be filled in by the editorial staff))

References

[1] V. R. Johnson, G. W. Vaughn, *J. Appl. Phys.* **1956**, *27*, 1173.
[2] R. D. Brown, R. A. Burton, P. M. Ku, *ASLE Trans.* **1964**, *7*, 236.
[3] G. Colas, A. Saulot, E. Regis, Y. Berthier, *Wear* **2015**, *330–331*, 448.
[4] N. Argibay, M. T. Dugger, B. A. Krick, J. F. Curry, B. Nation, A. Martini, N. C. Strandwitz, T. Babuska, *Tribol. Lett.* **2016**, *64*, 1.
[5] M. Rayman, Jet Propulsion Laboratory/NASA, **2013**.
[6] Space Exploration Technologies Corp. (SpaceX), **2015**.
[7] R. Cowen, *Nature* **2013**, *497*, 417.
[8] J. F. Curry, M. A. Wilson, H. S. Luftman, N. C. Strandwitz, N. Argibay, M. Chandross, M. A. Sidebottom, B. A. Krick, *ACS Appl. Mater. Interfaces* **2017**, *9*, 28019.
[9] G. Levita, A. Cavaleiro, E. Molinari, T. Polcar, M. C. Righi, *J. Phys. Chem. C* **2014**, *118*, 13809.
[10] Y. Morita, T. Onodera, A. Suzuki, R. Sahnoun, M. Koyama, H. Tsuboi, N. Hatakeyama, A. Endou, H. Takaba, M. Kubo, C. A. Del Carpio, T. Shin-yoshi, N. Nishino, A. Suzuki, A. Miyamoto, *Appl. Surf. Sci.* **2008**, *254*, 7618.
[11] S. Descartes, Y. Berthier, *Wear* **2002**, *252*, 546.
[12] M. Renouf, F. Massi, N. Fillot, A. Saulot, *Tribol. Int.* **2011**, *44*, 834.
[13] G. Colas, P. Serles, A. Saulot, T. Filleter, *J. Mech. Phys. Solids* **2019**, *128*, 151.
[14] Y. L. Su, W. H. Kao, *Tribol. Int.* **2002**, *36*, 11.
[15] T. W. Scharf, P. G. Kotula, S. V. Prasad, *Acta Mater.* **2010**, *58*, 4100.
[16] J. He, L. . Stals, J. . Celis, M. Van Stappen, P. Cosemans, X. Zhu, W. Lauwerens, *Surf. Coatings Technol.* **2002**, *163–164*, 422.
[17] K. J. Wahl, R. R. Chromik, G. Y. Lee, *Wear* **2008**, *264*, 731.
[18] I. L. Singer, S. D. Dvorak, K. J. Wahl, T. W. Scharf, *J. Vac. Sci. Technol. A Vacuum, Surfaces, Film.* **2003**, *21*, S232.
[19] G. Colas, A. Saulot, C. Godeau, Y. Michel, Y. Berthier, *Wear* **2013**, *305*, 192.
[20] N. N. Gosvami, J. Ma, R. W. Carpick, *Tribol. Lett.* **2018**, *66*, 1.
[21] L. E. Seitzman, R. N. Bolster, I. L. Singer, J. C. Wegand, *Tribol. Trans.* **1995**, *38*, 445.
[22] A. Savan, E. Pflüger, P. Voumard, A. Schröer, M. S. Paul, *Lubr. Sci.* **2000**, *12*, 185.
[23] E. O. Hall, *Nature* **1954**, *173*, 948.
[24] K. P. Furlan, J. D. B. de Mello, A. N. Klein, *Tribol. Int.* **2018**, *120*, 280.
[25] T. J. Rupert, C. A. Schuh, *Acta Mater.* **2010**, *58*, 4137.
[26] T. J. Rupert, J. C. Trenkle, C. A. Schuh, *Acta Mater.* **2011**, *59*, 1619.
[27] J. Wu, P. Cao, Z. Zhang, F. Ning, S. S. Zheng, J. He, Z. Zhang, *Nano Lett.* **2018**, *18*, 1543.
[28] Y. Mo, K. T. Turner, I. Szlufarska, *Nature* **2009**, *457*, 1116.
[29] B. N. J. Persson, O. Albohr, U. Tartaglino, A. I. Volokitin, E. Tosatti, *J. Phys. Condens. Matter* **2005**, *17*, DOI 10.1088/0953-8984/17/1/R01.
[30] J. F. Archard, *J. Appl. Phys.* **1953**, *24*, 981.
[31] V. Hegadekatte, S. Kurzenhäuser, N. Huber, O. Kraft, *Tribol. Int.* **2008**, *41*, 1020.
[32] I. P. Hayward, I. L. Singer, L. E. Seitzman, *Wear* **1992**, *157*, 215.
[33] Y. Zhao, X. Luo, H. Li, J. Zhang, P. T. Araujo, C. K. Gan, J. Wu, H. Zhang, S. Y. Quek, M. S. Dresselhaus, Q. Xiong, *Nano Lett.* **2013**, *13*, 1007.
[34] J. P. Oviedo, S. Kc, N. Lu, J. Wang, K. Cho, R. M. Wallace, M. J. Kim, *ACS Nano* **2015**, *9*, 1543.
[35] J. Moser, F. Levy, *J. Mater. Res.* **1993**, *8*, 206.
[36] S. Gangopadhyay, R. Acharya, A. K. Chattopadhyay, S. Paul, *Surf. Coatings Technol.* **2009**, *203*, 1565.
[37] J. T. Burwell, C. D. Strang, *J. Appl. Phys.* **1952**, *23*, 18.
[38] J. F. Archard, *J. Appl. Phys.* **1961**, *32*, 1420.
[39] W. S. Slaughter, Springer Science, Boston, MA, **1973**, pp. 46–78.

[40] J. L. Feldman, *Solid State Commun.* **1976**, *19*, viii.
[41] J. Musil, *Surf. Coatings Technol.* **2000**, *125*, 322.
[42] A. A. Voevodin, J. S. Zabinski, C. Muratore, *Tsinghua Sci. Technol.* **2005**, *10*, 665.
[43] C. Q. Chen, Y. T. Pei, K. P. Shaha, J. T. M. De Hosson, *J. Appl. Phys.* **2009**, *105*, DOI 10.1063/1.3130123.
[44] Q. Lu, N. Marks, G. C. Schatz, T. Belytschko, *Phys. Rev. B - Condens. Matter Mater. Phys.* **2008**, *77*, 1.
[45] G. He, J. Eckert, W. Löser, L. Schultz, *Nat. Mater.* **2003**, *2*, 33.
[46] R. Hauert, J. Patscheider, *Adv. Eng. Mater.* **2000**, *2*, 247.
[47] C. Popov, W. Kulisch, M. Jelinek, A. Bock, J. Strnad, *Thin Solid Films* **2006**, *494*, 92.
[48] G. Colas, A. Saulot, N. Bouscharain, C. Godeau, Y. Michel, Y. Berthier, *Tribol. Int.* **2013**, *65*, 177.
[49] M. Godet, *Wear* **1984**, *100*, 437.
[50] Y. Berthier, *Third Body Reality - Consequences and Use of the Third-Body Concept to Solve Friction and Wear Problems*, **2005**.
[51] V. P. Kazachenko, V. V. Popov, A. M. Dubravin, H.-S. Ahn, S. A. Chizhik, *Wear* **2002**, *249*, 617.
[52] J. Ye, M. Kano, Y. Yasuda, *J. Appl. Phys.* **2003**, *93*, 5113.
[53] S. Mignuzzi, A. J. Pollard, N. Bonini, B. Brennan, I. S. Gilmore, M. A. Pimenta, D. Richards, D. Roy, *Phys. Rev. B - Condens. Matter Mater. Phys.* **2015**, *91*, 1.
[54] N. T. McDevitt, J. E. Bultman, J. S. Zabinski, *Appl. Spectrosc.* **1998**, *52*, 1160.
[55] G. L. Frey, R. Tenne, M. J. Matthews, M. S. Dresselhaus, G. Dresselhaus, *Phys. Rev. B - Condens. Matter Mater. Phys.* **1999**, *60*, 2883.
[56] K. Zhang, S. Hu, Y. Zhang, T. Zhang, X. Zhou, Y. Sun, T. X. Li, H. J. Fan, G. Shen, X. Chen, N. Dai, *ACS Nano* **2015**, *9*, 2704.
[57] D. Doratotaj, J. R. Simpson, J. A. Yan, *Phys. Rev. B* **2016**, *93*, 1.
[58] C. Muratore, J. E. Bultman, S. M. Aouadi, A. A. Voevodin, *Wear* **2011**, *270*, 140.
[59] J. E. Sader, J. W. M. Chon, P. Mulvaney, *Rev. Sci. Instrum.* **1999**, *70*, 3967.
[60] C. P. Green, H. Lioe, J. P. Cleveland, R. Proksch, P. Mulvaney, J. E. Sader, *Rev. Sci. Instrum.* **2004**, *75*, 1988.
[61] R. J. Cannara, M. Eglin, R. W. Carpick, *Rev. Sci. Instrum.* **2006**, *77*, DOI 10.1063/1.2198768.
[62] N. M. U. Renevier, V. C. Fox, D. G. Teer, J. Hampshire, *Surf. Coatings Technol.* **2000**, 24.
[63] S. Domínguez-Meister, T. C. Rojas, M. Brizuela, J. C. Sánchez-López, *Sci. Technol. Adv. Mater.* **2017**, *18*, 122.
[64] J. Mayer, L. A. Giannuzzi, T. Kamino, J. Michael, *MRS Bull.* **2007**, *32*, 400.
[65] S. Plimpton, *J. Comput. Phys.* **1995**, *117*, 1.
[66] T. Liang, S. R. Phillpot, S. B. Sinnott, *Phys. Rev. B - Condens. Matter Mater. Phys.* **2009**, *79*, 1.
[67] M. Li, Y. Wan, L. Tu, Y. Yang, J. Lou, *Nanoscale Res. Lett.* **2016**, *11*, 0.
[68] S. Xiong, G. Cao, *Nanotechnology* **2015**, *26*, DOI 10.1088/0957-4484/26/18/185705.
[69] C. H. Rycroft, **2009**, 1.
[70] E. Polak, *Computational Methods in Optimization: A Unified Approach*, Academic Press, New York, **1971**.

Figures

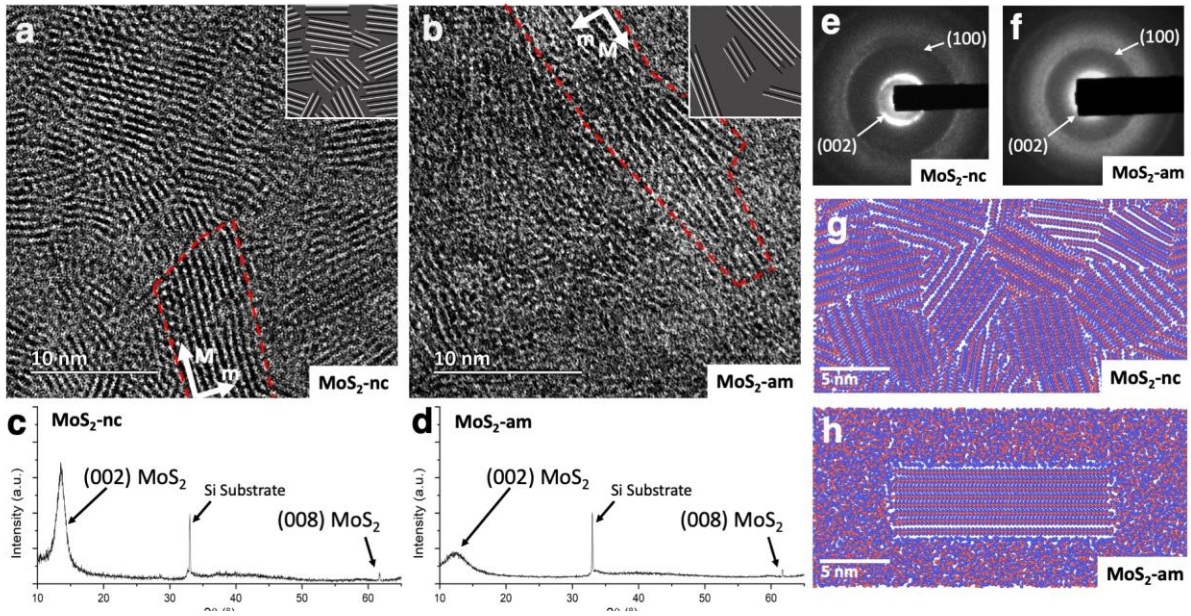

Figure 1. Nanocrystalline MoS_2 material characterization and molecular dynamics unit cells; Cross-sectional HRTEM micrograph and schematic representation of a) MoS_2-nc, b) MoS_2-am, nanocrystal structure outlined with dotted red line and major (M) and minor (m) axes shown; XRD patterns of c) MoS_2-nc, d) MoS_2-am; Selected area diffraction patterns of e) MoS_2-nc, f) MoS_2-am; Molecular dynamics simulation unit cells for g) MoS_2-nc, h) MoS_2-am

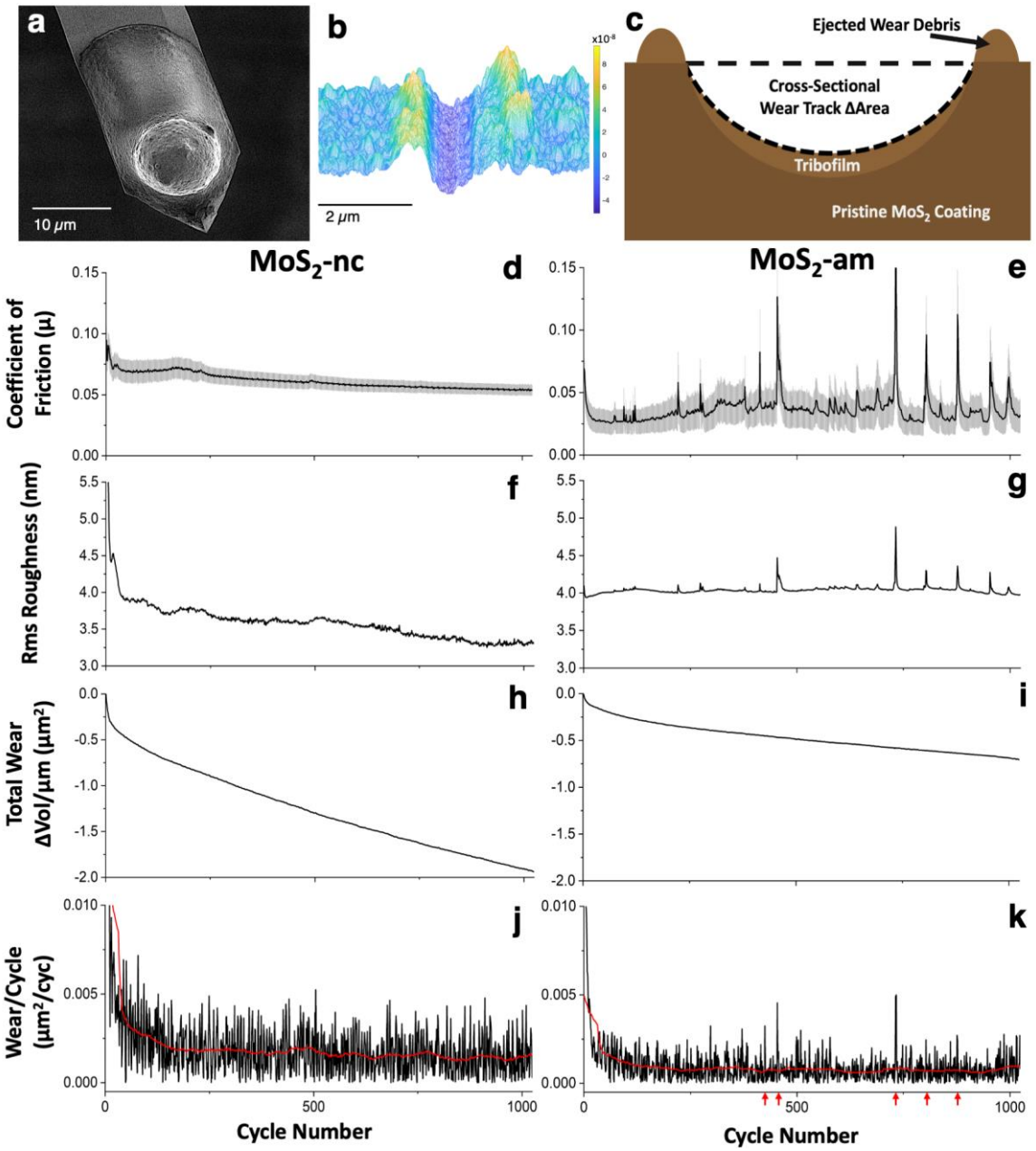

Figure 2. Tribological characteristics of MoS_2 coatings by friction force microscopy; a) AISI 440C steel bead attached to a high-stiffness (64 ± 4 N/m) AFM cantilever; b) AFM image of MoS_2-nc wear track following 1024 cycles; c) Schematic representation of cross-sectional wear track profile following FFM; MoS_2-nc figures shown left and MoS_2-am right: d & e) Coefficient of friction evolution (black) with standard deviation (grey); f & g) Rms roughness evolution; h & i) Cumulative wear volume per μm travelled; j & k) Wear volume change per cycle (black) with moving average (red); Red arrows along the X axis of k) indicate the position of statistical outliers; Error for Rms (f & g): ±0.08 nm, Error for Wear (h-k): $\pm 3.5E^{-4}$ μm^2.

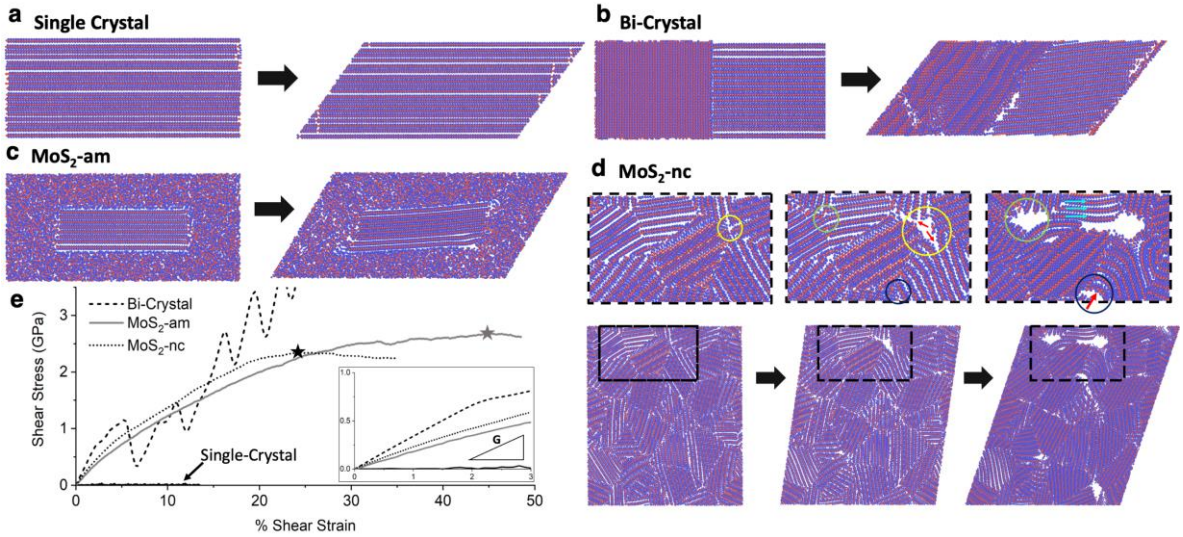

Figure 3. Molecular dynamics simulations of MoS_2 crystals within different structures under shear deformation; a) Single-crystal MoS_2; b) Bi-crystal of two MoS_2 crystals oriented at 90º to each other; c) Nanocrystal embedded in an amorphous matrix as per MoS_2-am; d) Polycrystalline sample with 6 nm average grain size as per MoS_2-nc; e) Shear stress and shear strain curves for the four samples with Ultimate Shear Stress noted with stars on MoS_2-am and MoS_2-nc, inset showing the linear-elastic regime up to 2% shear strain

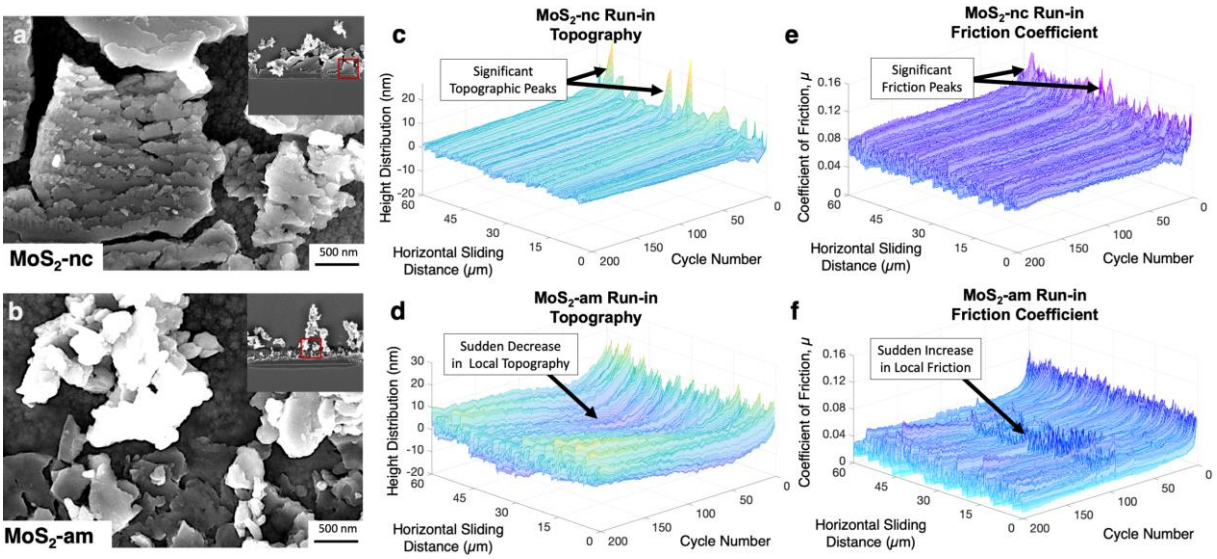

Figure 4. Run-in wear, topographic, and frictional characteristics; Wear debris following 150 cycles at the edge of the wear track for a) MoS_2-nc, b) MoS_2-am; 3D mapping of run-in friction and topographic characteristics of c) MoS_2-nc topography, d) MoS_2-am topography, e) MoS_2-nc friction coefficient; f) MoS_2-am friction coefficient

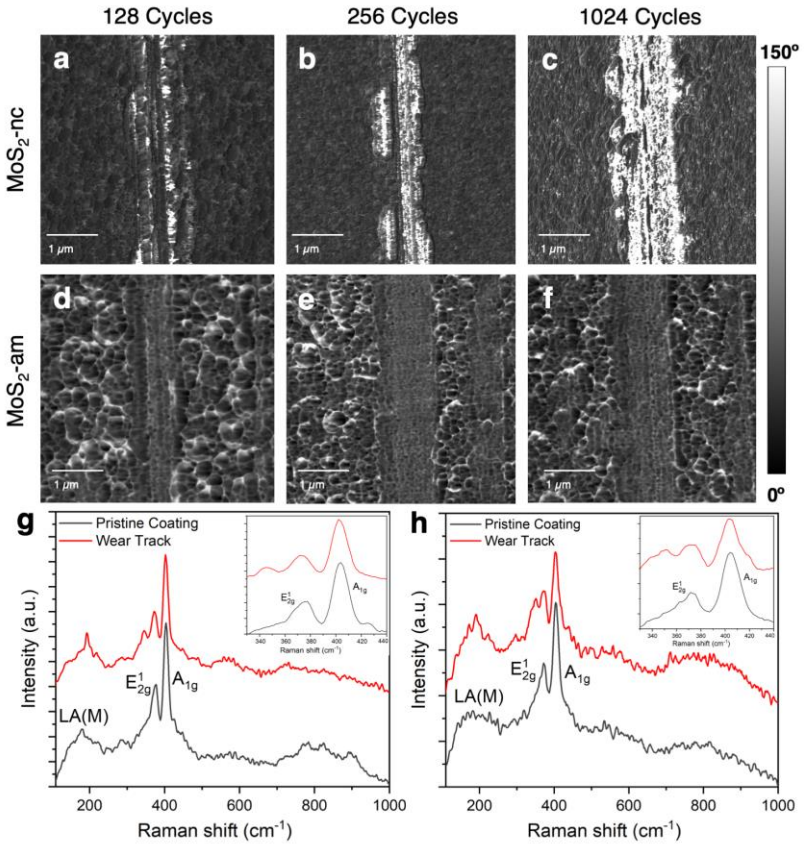

Figure 5. AFM tapping mode phase imaging of the FFM wear track following 128, 256, 1024 cycles; a-c) MoS_2-nc after 128, 256, 1024 cycles, and d-f) MoS_2-am after 128, 256, 1024 cycles respectively; g) Raman spectrum for MoS_2-nc and h) Raman spectrum of MoS_2-am with insets highlighting $E^1_{2\,g}$ and A_{1g} peaks

Tables

Table 1. Raman spectrum analysis of MoS_2-nc and MoS_2-am for the pristine coating and inside the wear track after 1024 cycles of FFM

		$E^1_{2\,g}$ Peak		A_{1g} Peak		LA(M) Peak
		FWHM (cm^{-1})	Peak Location (cm^{-1})	FWHM (cm^{-1})	Peak Location (cm^{-1})	Intensity ($I_{LA(M)}/I_{A1g}$)
MoS_2-am	Pristine	16.2	373.2	15.2	405.1	0.92
	Wear	20.0	372.5	16.1	404.9	1.39
MoS_2-nc	Pristine	16.2	373.4	14.2	404.1	1.05
	Wear	15.2	372.7	13.3	403.2	1.16

In situ Friction Force Microscopy and molecular dynamic simulations reveal the true wear and friction mechanics of two nanostructured MoS_2 coatings when subjected to shear forces. Despite similar macroscopic mechanical properties, purely nanocrystalline and nanocrystal-amorphous coatings exhibit entirely different wear, crack propagation and failure behaviour.

Keyword: Nano-Mechanics

P. Serles, H. Sun, G. Colas, J. Tam, E. Nicholson, G. Wang, J. Howe, A. Saulot,

C. V. Singh, T. Filleter**

Structure Dependent Wear and Shear Mechanics of Nanostructured MoS_2 Coatings